

Short Communication

Effects of Heat Treatment on Microstructure and Properties of Inconel625 Alloy Blades Prepared by Selective Laser Melting

Mengting Zhang^{1,2}, Xinghua Liang³, Xiaofeng Zhang², Min Liu², Qingkun Chu^{2,4}, Xi Zhou⁴

¹ School of Automotive Engineering, Liuzhou Vocational & Technical College, Liuzhou, China;

² Guangdong Institute of New Materials, National Engineering Laboratory for Modern Materials Surface, Guangdong Academy of Science, Guangzhou, China

³ Guangxi Key Laboratory of Automobile Components and Vehicle Technology, Guangxi University of Science & Technology, Liuzhou, China;

⁴ School of Materials and Energy, Guangdong University of Technology, Guangzhou, China

*E-mail: 475389617@qq.com

Received: 26 September 2021 / Accepted: 29 October 2021 / Published: 6 December 2021

Inconel625 alloy blades were prepared by selective laser melting (SLM). Optical microscope (OM), scanning electron microscope (SEM), electron backscatter diffraction (EBSD), energy dispersive spectrometer (EDS) analysis techniques were employed to study the microstructure and properties under as-prepared and heat-treated conditions. The results show that the density of the as-prepared blades is as high as 99.9%. The microscopic morphology exhibits obvious anisotropy with an angle of 67° between two adjacent layers. MC granular phase and γ phase are generated during solidification. The microstructures of blades at different positions are similar, which shows that the support design and production sequence during the preparation process have small effect on them. After heat treatment at 900°C for 4h, anisotropy with an angle of 67° of as-prepared blades disappeared and new uniform crystal grains and Mo-rich phase area are discovered instead, and also with the improved corrosion resistance.

Keywords: SLM; Inconel625; blades; heat-treated

1. INTRODUCTION

Inconel625 alloy is a nickel-based superalloy that achieves solid solution strengthening by adding elements such as Nb, Mo, and Cr to the nickel-based face-centered cubic structure. The alloy has excellent properties such as high strength, corrosion resistance, high temperature oxidation resistance, etc. [1], and is widely used in aerospace, automotive, chemical and other fields. The traditional way, which including casting metallurgy technology, powder metallurgy technology and spray forming technology, is difficult to prepare high-precision and complex Inconel625 alloy parts, and it is also with

long production cycles and low material utilization.

Selective Laser Melting (SLM) technology is a kind of additive technology, which is first with computer software to slice and layer 3D digital model of the parts and then with the high-energy laser beam to selectively melt the metal powder layer by layer according to the profile data [2]. By spreading powder layer by layer, melting, solidifying and accumulating layer by layer, the three-dimensional solid parts are prepared at last. SLM technology can complete the preparation of complex parts in a short time, with simple operation and high material utilization [3,4].

M.J. Ansari et al. discussed the temperature distribution of surface and molten pool in the SLM process through model calculations and experiments. When the power and scanning speed were 150 W and 750 mm/s respectively, the center point was as high as 2530.9 K, and the melting center point temperature gradually decreased as it is farther from the light spot [5]. M.A. Balbaa et al. studied the influence of SLM process parameters on the surface and molten pool structure and residual stress of Inconel625 alloy. The density was greater than 97%, and the surface residual stress was between 50-550 MPa [6]. J. Lee et al. studied the influence of heat treatments on mechanical properties of the Inconel625 alloy prepared by SLM. The mechanical properties performed more stable and excellent comprehensive after heat treatment when tested at the temperature of 500°C, 600°C, and 700°C respectively [7]. The quantity of precipitated phases for Inconel625 alloy was affected by the forming process, solidification cooling rate, holding temperature, time, and stress. The phase evolution of different forming methods and heat treatment methods was different [3,8,9].

At present, main research on SLM forming specimens at home and abroad was rectangular or tensile workpiece specimens prepared, and also process parameters, molten pool, and mechanical properties discussed [10-12], but the preparation of complex parts by SLM and the performance of different positions for the parts are rarely reported.

In this paper, the complex parts of Inconel625 aircraft engine blades were prepared by SLM method, and microstructure of blades before and after heat treatment were studied by optical microscope OM, scanning electron microscope (SEM), backscatter electron microscope (EBSD), energy spectrum analyzer (EDS) and other test methods. At the same time, the performance of electrochemical corrosion was compared and analyzed by the electrochemical workstation.

2. EXPERIMENT

2.1 Feedstock materials

The powder of Inconel625 alloy provided by Carpenter Technology Corporation was used as the feedstock materials, and its chemical composition is shown in Table 1. The powder morphology is shown in Figure 1. It can be seen that the powder has high sphericity and a small amount of star-shaped powder around the powder. The particle size of the powder ranges from 5 μ m to 45 μ m, and the average crystal size is 20.6 μ m.

Table 1. Chemical composition of Inconel625 power (wt%)

| Elements | Ni | Cr | Mo | Nb | Fe | Si | Mn | Al | Ti | Co | C | P | S |
|----------|------|----|----|------|-----|-----|-----|-----|-----|-----|-----|-------|-------|
| Content | Bal. | 20 | 8 | 3.15 | 5 | 0.5 | 0.5 | 0.4 | 0.4 | 1 | 0.1 | 0.015 | 0.015 |
| | | - | - | - | max | max |
| | | 23 | 10 | 4.15 | | | | | | | | | |

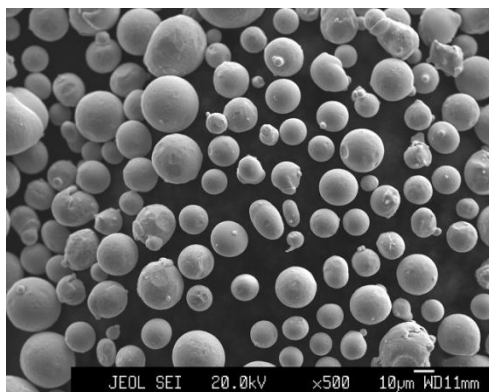


Figure 1. SEM image of Inconel625 power

2.2 The process of SLM for blades

The process of SLM for blades is shown in Figure 2. The 3D CAD model of the parts was sliced and layered, and the support structure design was carried out on the computer. Then, the data of computer was imported into the SLM equipment. The layers of powder were remelted and solidified by the laser spot, and a solid blades was formed finally[13].

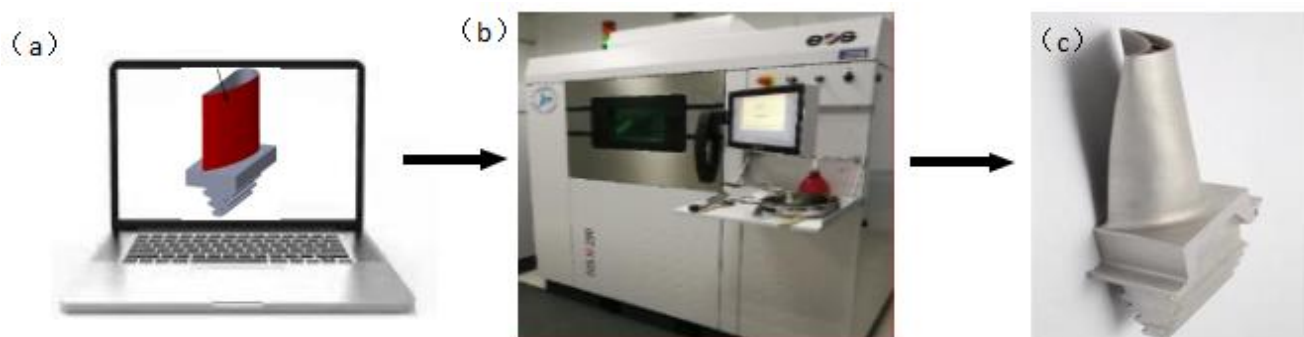


Figure 2. The Process of SLM for blades (a) theoretical CAD model (b) preparation process (c) as-prepared blade

The SLM equipment M290 is used to prepare blades, which is produced by the Germany EOS company. The equipment is equipped with a laser with a maximum power of 400W, a spot diameter of 100µm, and a maximum scanning speed of 7m/s [14]. The process parameters of SLM for blades are shown in Table 2. The energy density of the laser is calculated to be 75 J.mm⁻³ according to the energy

density formula $E=P/HVD$.

Table 2. The process parameters of SLM

| Process parameters | Power (W) | Scan speed (mm/s) | Scan pitch (mm) | Thickness of powder layer (mm) |
|--------------------|-----------|-------------------|-----------------|--------------------------------|
| Value | 300 | 1000 | 0.1 | 0.04 |

2.3 Heat treatment

The KBF13Q atmosphere box furnace produced by Nanda was used for heat treatment of the blades. The blades were heat-treated at 900°C with the heating rate of 20°C/min for 4 h, and followed by furnace cooling.

2.4 Microstructure characterization

Blades for microstructure were sectioned by the DK7763 wire cutting machine. As shown in the figure, specimen 1# is the section of as-prepared blades (prepared by SLM), cut at a height of 5mm along the Z direction. In this position, there is an auxiliary support structure for the blades during the preparation process (the blue area in Figure 3). Specimen 2# is the section of as-prepared blades, cut at a height of 30mm along the Z direction. Specimen 3# is the heat-treated blades section, cut at a height of 5mm along the Z direction.

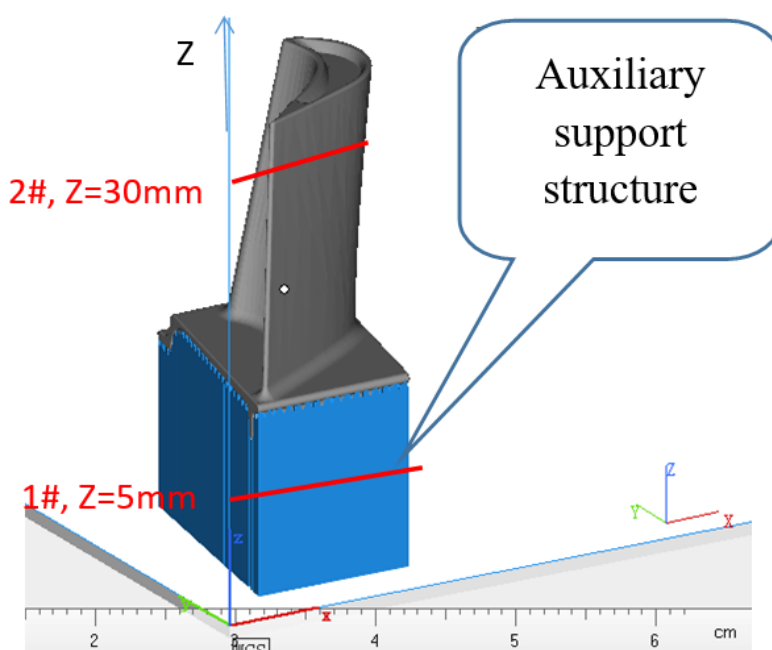


Figure 3. Illustration of blade cutting in the Z direction

Specimens for microstructure analyses were hot mounted in phenolic resin by the machine of XQ-2B metallographic inlaying. And conventionally grounded with SiC abrasive papers and polished with diamond paste until the surface reaches a mirror effect by the machine of Tegra Min-25. The polished surface of specimens was etched with a mixed solution (the volume ratio of HNO₃ to HCL is 1:3) for about 10 seconds until a snowflake-like appearance appeared. The Leica DMI300M optical microscope (OM) was used to observe the metallography of specimens and combined with Image software to analyze the relative density of the specimens. The JSM-7610FPlus scanning electron microscope equipped with EBSD (Electron Backscattered Diffraction) probe and EDS (Energy Dispersive Spectrometer) was used for organization morphology and composition analysis.

2.5 Electrochemical experiment

The blades were cut into a specimen with a size of 15mm × 10mm × 5mm, and the specimens were welded with wire. The non-test surface of specimens were sealed with epoxy resin, and the test surface were polished with sandpaper and diamond, and then used as a working electrode after ultrasonic cleaning. The electrochemical test was conducted in a three electrode electrochemical cell (50 mL), and with about 30 mL of test solution by using an electrochemical workstation (CorrTest-CS350H). Inconel625 specimens (with an exposed area of 1.5cm² in the tested solution), Calomel (KCl saturated) and platinum plate and were used as the working electrode (W.E.), the reference electrode (R.E.) and the counter electrode (C.E.), respectively. In order to study the corrosion performance of as-prepared blade and heat-treated blade in acidic environment, the HCl solution with pH=3 was used as the solution for corrosion investigation [15]. The electrochemical test were performed at a scan rate of 1 mV/s at room temperature, and the Tafel curves were used to characterize the corrosion performance of prepared blade and heat-treated blade.

3. RESULTS AND DISCUSSION

3.1 Microstructure characterization on the as-prepared blades

Figure 4(a) is the OM images of the as-prepared blades (1#, Z=5mm). No obvious defects, such as pores, cracks, and poor fusion, are observed in the picture, which indicate that the blades prepared by SLM technology is with good metallurgical bonding, uniform and dense microstructure. Combined with Image software analysis, and found that the density is more than 99.9%.

The microscopic morphology exhibits obvious anisotropy with an angle of 67° between two adjacent layers. It is because that, in the SLM process, as shown in Figure 5, first the 0.04mm metal powder was spread in (n-1)th layer with a horizontal scraper, selectively melted with the high-energy laser beam according to the data information of the current layer. Then spread and melted another 0.04mm metal powder in nth layer. The laser spot direction of each adjacent layer rotated 67° and the powder melted layer-by-layer until the entire part is prepared.

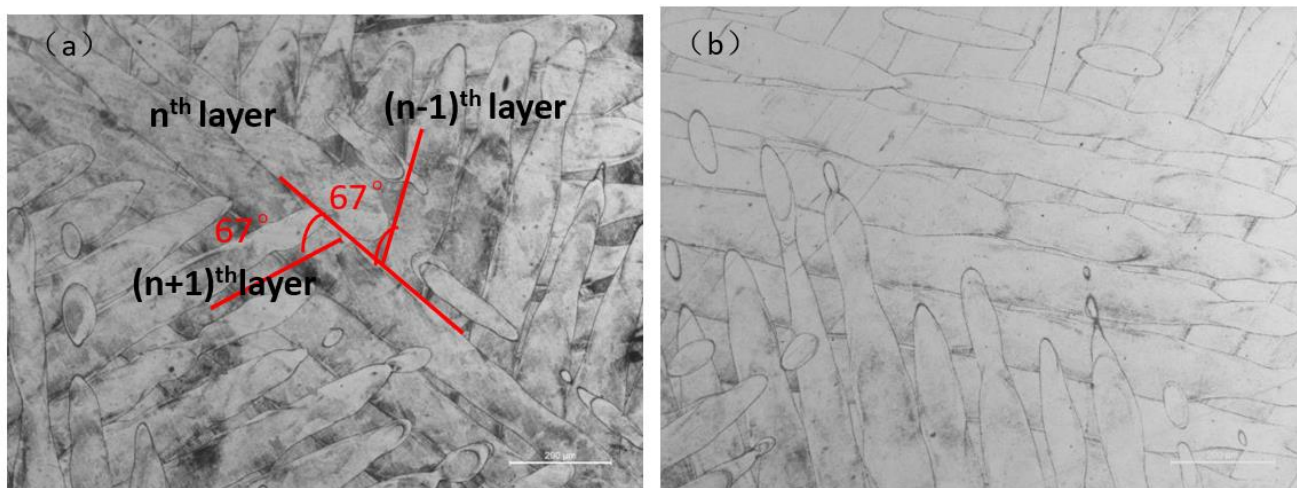


Figure 4. OM images of as-prepared blades (a)1#, Z=5 mm, (b) 2# ,Z=30 mm

The linear morphology in the figure 4(a) is the solidification bond line of the alloy between different laser melting channels and different layers, which is the boundary of the molten pool [5]. The maximum width of each melt channel is measured to be about 100um, which is mainly determined by the diameter of the scanning spot.

Figure 4(b) is the OM images of the as-prepared blades (2#, Z=30mm). In the picture, the microstructure is observed to be similar with those at Z=5mm. Combined with software analysis, it is found that the density is more than 99.9% too.

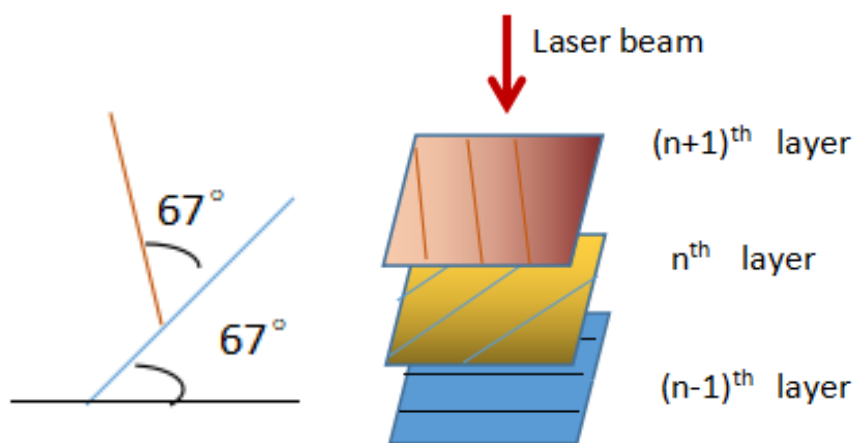


Figure 5. Selected laser scanning strategies of SLM process

Figure 6(a)(b) is the SEM images of the as-prepared blades (1#, Z=5mm), The bright white linear area is the boundary of the molten pool as shown in Figure 6(a). Figure 6(b) is a detailed view of Figure 6(a). Obviously, the larger boundary particles are discontinuous precipitation. According to the principle of secondary electron imaging, the formation of contrast depends on the different angles of the uneven surface of the specimens with respect to the incident electron beam, thereby reflecting different secondary electron beams [16]. It shows that the particle shape is convex in the SEM image, which indicates that the particle shape has strong wear resistance during the grinding and polishing process.

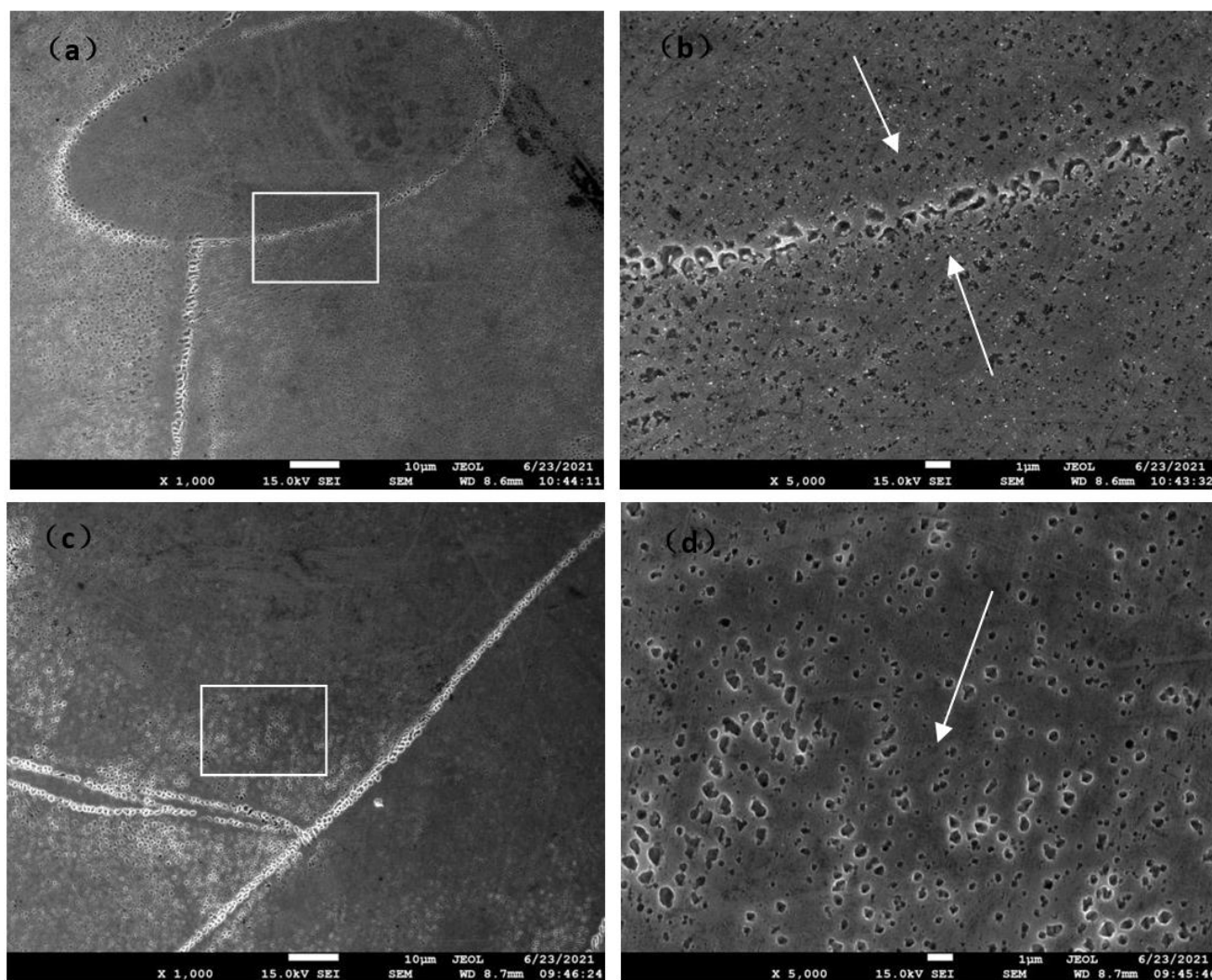


Figure 6. SEM images of as-prepared blades (a) 1#, $Z=5\text{ mm} \times 1000$, (b) 1#, $Z=5\text{ mm} \times 5000$, (c) 2#, $Z=30\text{ mm} \times 1000$, (d) 2#, $Z=30\text{ mm} \times 5000$

There are also partially dispersed granular precipitates in the molten pool. As shown in figure 6(b) by the arrow, the closer to the boundary of the molten pool, it tends to be the more and the larger of particles. It is because the powder absorbs the heat of the laser beam and melts into a liquid phase and gradually dissipates heat, thereby forming different temperatures in the molten pool. Generally, the temperature inside the molten pool is higher, and the temperature at the edge of the molten pool is lower [17]. The heat exchange between the molten pools, the molten channels and layers during the laser melting process also leads to different morphologies [17]. Each molten pool is in a different cross-section when grinding and polishing during preparation of specimens, so that it is observed that the particle size and morphology are different in Figure 6(a).

Figure 6(c)(d) is the SEM images of the as-prepared blades (2#, $Z=30\text{mm}$). In the images, the detailed microstructure is observed to be similar with Figure 6(a)(b) (1# $Z=5\text{mm}$) which the particles show a gradual increase trend from the inside of the molten pool to the boundary. Combining the OM and SEM images, it can be concluded that the microstructure is less affected by auxiliary support

structure during preparation process and by the prepared sequence.

During the cooling process of Inconel625 alloy, from liquid L, $L \rightarrow \gamma$ reaction occurred in the initial solidification stage, $L \rightarrow \gamma + MC$ reaction occurred in the stable solidification stage (M mainly refers to Nb and Ti), and finally a small amount of residual liquid was slowly solidified due to component segregation in the solidification process, the $L \rightarrow \gamma + \text{Laves}$ reaction occurred [18]. The reactions affected by the cooling rate [15]. Due to the small melting area (laser spot diameter 100 μm , layer thickness 0.04 mm) and fast scanning speed (1000 mm/s) during the SLM preparation process, the alloy powder melts and cools rapidly, which lead to the first two reactions mainly occur. The matrix phase is γ , and the granular area is MC phase [19].

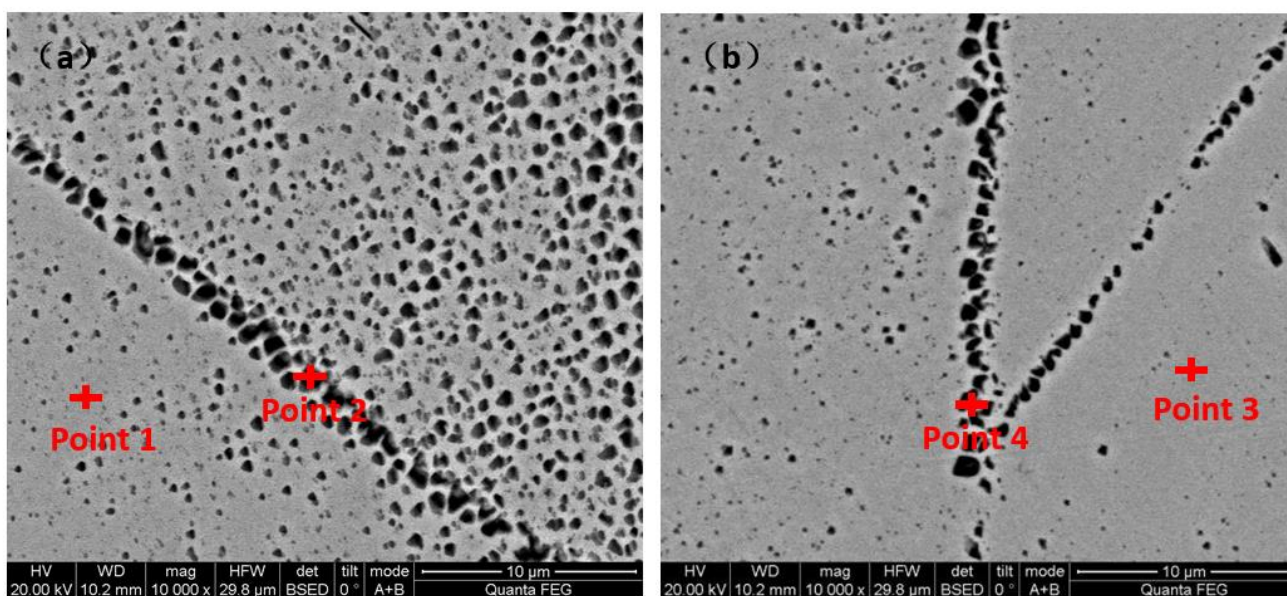


Figure 7. EBSD images of as-prepared blades (a) 1#, Z=5 mm, (b) 2#, Z=30 mm

Table 3. Elemental composition of different area points (wt%)

| Specimens | Area | C | Nb | Mo | Cr | Ni |
|------------|----------------------|------|------|------|-------|-------|
| 1#, Z=5mm | Point 1 (gray) | 3.49 | 4.32 | 9.37 | 19.97 | 62.84 |
| | Point 2 (deep black) | 2.77 | 3.71 | 8.54 | 20.26 | 64.72 |
| 2#, Z=30mm | Point 3 (gray) | 2.32 | 3.97 | 9.00 | 20.67 | 64.03 |
| | Point 4 (deep black) | 2.54 | 3.75 | 8.09 | 20.38 | 65.25 |

Since the phase transition mechanism of the solidification process belongs to the nucleation and growth mechanism, different driving forces and resistances at different points prompt different nucleation probabilities. Affected by temperature and cooling rate in different areas of the molten pool,

the nucleation position and growth speed of the two phases are different [18]. And it is the root cause that the number and size distribution of granular MC phases are clearly observed different in the figure 6.

The EDS spectrometer is used to test the content of elements. Figure 7 is the EBSD images of the as-prepared blades. In order to reduce the deviation, multi-point measurement was selected as shown in the table 3. The result shows that there are little difference in composition of C, Nb, Mo, Cr and Ni in different point. This is because the spot area of SLM forming is small, and each molten pool is small and cooled rapidly, and the components are too late to migrate to form segregation in an element-rich area.

3.2 Microstructure evolution of the heat-treated blades

Figure 8(a) is the OM image of the blades after heat treatment. The original anisotropy with an angle of 67° between two adjacent layers disappeared and replaced by a uniform grain morphology. It is due to the high speed of the SLM process, resulting in segregation and stress in the molten pool.

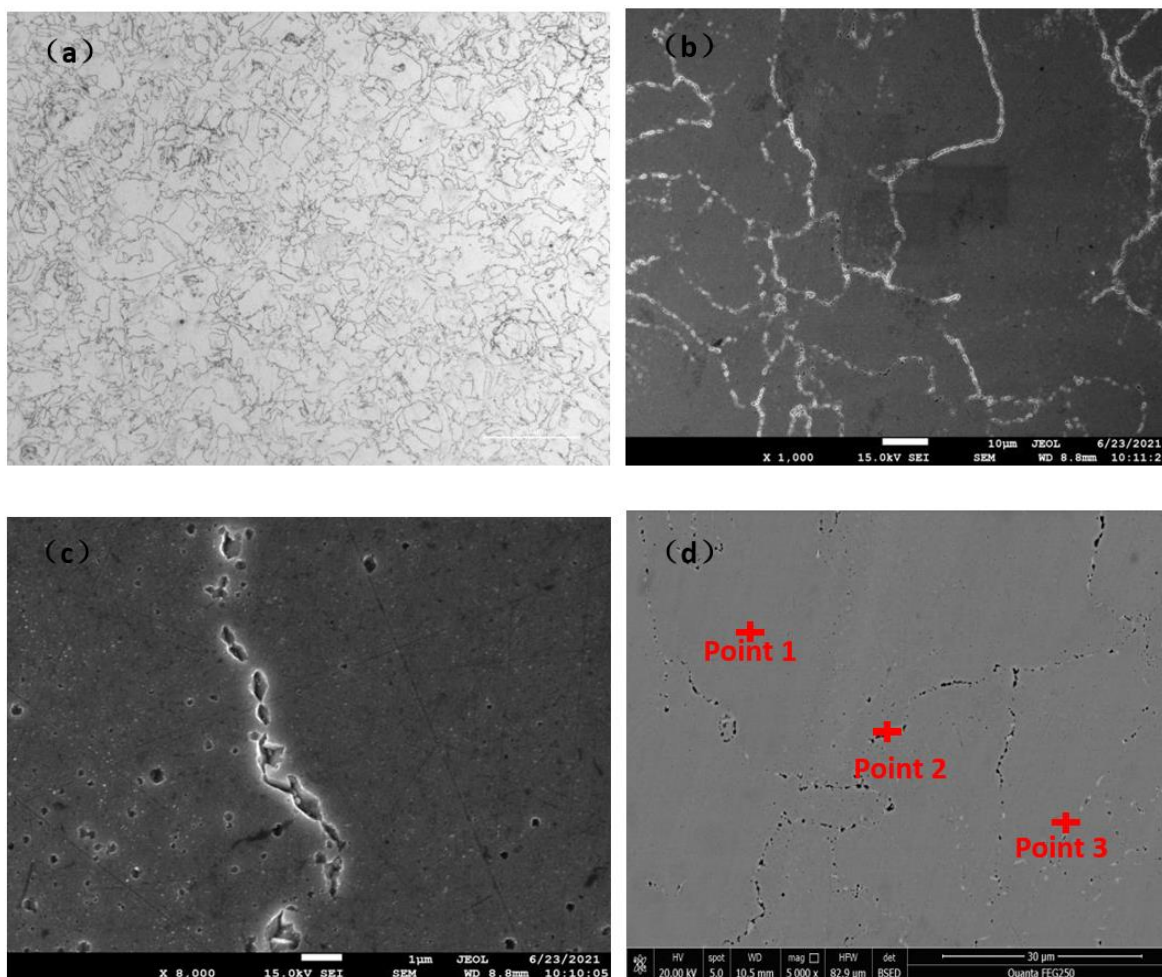


Figure 8. Microstructure image of the heat-treated blades (a) OM, (b) SEM , $\times 1000$, (c) SEM, $\times 8000$, (d) EBSD

Stress release occurs through long-term heat treatment, and the internal structure undergoes atomic diffusion to regenerate new crystal grains under the impetus of temperature and stress. Accompanied by the migration of the grain boundary, the concave surface moves in the growth direction, and finally, the intersection angle between three adjacent grains is almost equal and close to 120° as shown in Figure 8(b). Figure 8(c) is a detailed SEM image of Figure 8(b). It can be seen that the grain boundaries are island-shaped discontinuous granular phases, and the crystals are also dispersed and distributed in smaller granular phases.

Combined with the EBSD image in Figure 8(d), it is found that there are two contrast phase regions in the island particles in the grain boundaries, which are different from only one phase zone in the grain boundary before heat treatment. Similarly, the small particles dispersed inside the crystal also show two different contrast phases. It is because in the process of atomic diffusion, different regions form different atomic ratios under different conditions. The backscattered electrons reflect the characteristics of composition through the contrast of the atomic number. Large average atomic number produces a stronger backscattered electron signal, forming a brighter area, and a lower average atomic number forms less backscattered electrons, forming a darker area [20].

Through the energy spectrum of the composition area of different contrast analysis, the results are shown in Table 4. There was little difference in the composition of the C element in the three areas. The Nb element content in the dark black and bright white areas were 6.07% and 7.04%, respectively, which was higher than that in the gray area (Nb3.56%). The content of Mo in the bright white area increased significantly to 18.3%. It shows that the content of the C element is relatively uniform, and an Nb-rich phase region is formed through the heat treatment. In other words, the bright white area is rich in Mo elements.

Table 4. Heat-treated blades composition of different area (wt%)

| Area | C | Nb | Mo | Cr | Ni |
|------------------------------|------|------|-------|-------|-------|
| Point 1 (Gray area) | 3.53 | 3.56 | 8.85 | 20.09 | 63.99 |
| Point 2 (Dark black area) | 4.79 | 6.07 | 8.02 | 16.85 | 64.27 |
| Point 3 (White area) | 4.96 | 7.04 | 18.30 | 18.97 | 50.74 |

3.3 Electrochemical performance

In order to study the corrosion performance of as-prepared blade and heat-treated blade in the HCl solution with pH=3, the polarization curves of the specimens were obtained by electrochemical test as shown in the figure 9. After heat treatment, the cathode area of the specimen was obviously polarized, and the anode area changed with the potential. By the cathodic polarization extrapolation method, the self-corrosion potential of as-prepared blade is -0.493V, and the self-corrosion current is $8.02 \times 10^{-6} \text{A/cm}^2$. After heat treatment, the self-corrosion potential is -0.259V, and the self-corrosion current is $4.002 \times 10^{-6} \text{A/cm}^2$.

$7\text{A}/\text{cm}^2$. Due to the heat-treated blade plays higher corrosion potential and lower corrosion current density, from a thermodynamic point of view, the heat-treated blade are more resistant to corrosion than the as-prepared blade. Compared with the polarization curve of Inconel 625 studied by X. Li et al. [15], it is found that the heat-treated blade in this paper also plays higher corrosion potential and lower corrosion current density.

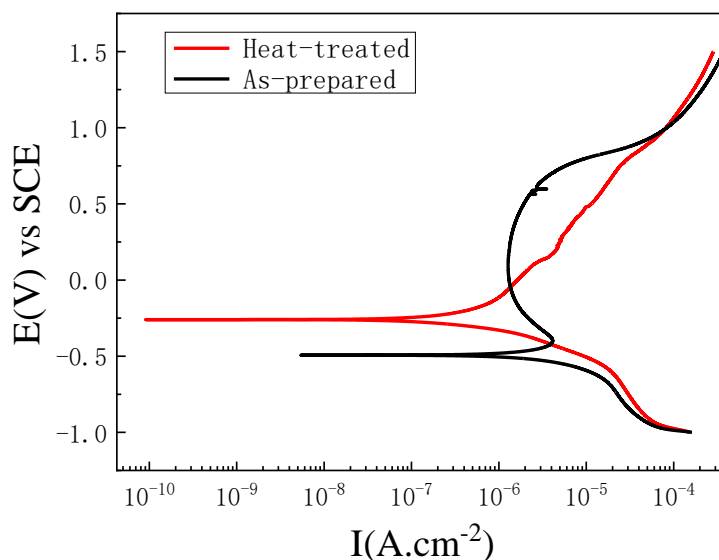


Figure 9. Polarization curve of as-prepared blade and heat-treated blade in a HCl solution with pH=3

4. CONCLUSIONS

The density of the as-prepared blades is as high as 99.9%. The microscopic morphology exhibits obvious anisotropy with an angle of 67° between two adjacent layers. MC granular phase and γ phase are generated during rapid cooling and final solidification. From the inside of the molten pool to the boundary, the granular distribution of MC phase gradually increased.

(1) The microstructures of blades at different positions are similar, which shows that the support design and production sequence during the preparation process have small effect on them.

(2) After heat treatment for 4h at 900°C , anisotropy with an angle of 67° of as-prepared blades disappeared and new uniform crystal grains and Mo-rich phase area are discovered instead. The black granular phase and the Mo-rich bright white phase are dispersed in the crystal interior and grain boundaries.

(3) According to the electrochemical test, the self-corrosion potential of as-prepared blades is -0.493V , and the self-corrosion potential of heat-treated blades is -0.259V . The heat-treated blades are more resistant to corrosion than the as-prepared blades.

ACKNOWLEDGEMENTS

The research work received the special fund project of Guangdong Academy of Sciences for the implementation of innovation-driven development capacity building(No.2018GDASCX-0402) ,and the special scientific research fund of Guangxi Liuzhou Vocational and Technical College(No.2021)

References

1. S. Floueen, G. E. Fuchs and W. J. Yang, *Miner. Met. Mater. Ser.*, 2 (1994)13-37
2. J. Kozak and T. Zakrzewski, *AIP Conf. Proc. (USA)*, 2017 (2018) 020010.
3. T. DebRoy, H.L. Wei, J.S. Zuback, T. Mukherjee, J.W. Elmer, J.O. Milewski, A.M. Beese, A. Wilson-Heid, A. De and W. Zhang, *Prog. Mater. Sci.*, 92 (2018) 112-224.
4. B. Lu, *China Mechanical Eng.*, 31 (2020) 19-23.
5. M. J. Ansari, D. S. Nguyen and H.S. Park, *Materials*, 12 (2019)1272.
6. M. A. Balbaa, M.A. Elbestawi and J. McIsaac, *Int. J. Adv. Manuf. Tech.*, 104 (2019) 3511-3529.
7. J. Lee, M. Turner, S. Jun, H.U. Hong, E. Copin and P. Lours, *Mat. Sci. Eng A-Struct.*, 790 (2020) 139720.
8. C.O. Yenusah, Y. Ji, Y. Liu, T.W. Stone, M.F. Horstemeyer, L.-Q. Chen and L. Chen, *Comp. Mater. Sci.*, 187 (2021) 110123.
9. X.Y. Fang, H.Q. Li, M. Wang, C. Li and Y.B. Guo, *Mater. Charact.*, 143 (2018) 182-190.
10. Y. Hu, X. Lin, Y. Li, S. Zhang, Q. Zhang, W. Chen, W. Li and W. Huang, *Mat. Sci. Eng A-Struct.*, 817 (2021) 141309.
11. C. Li, R. White, X.Y. Fang, M. Weaver and Y.B. Guo, *Mat. Sci. Eng A-Struct.*, 705 (2017) 20-31.
12. S. Li, Q. Wei, Y. Shi, Z. Zhu and D. Zhang, *J. Mater. Sci. Technol.*, 31 (2015) 946-952.
13. R. Ponche, O. Kerbrat, P. Mognol and J.Y. Hascoet, *Robot. Com.-Int. Manuf.*, 30 (2014) 389-398.
14. X. Chen, G. Zhao, D. Dong, W. Ma, Y. Hu and M. Liu, *Chin. J Lasers*, 46 (2019) 1202002.
15. X. Li, D. Yi, B. Liu, J. Zhang, X. Yang, C. Wang, Y. Feng, P. Bai, Y. Liu and M. Qian, *Mat. Sci. Eng. A-Struct.*, 798 (2020) 140099.
16. L. Chen, J. Xu and J. Chen, *Sci. China Earth Sci.*, 58 (2015) 1768-1778.
17. Z. J. Fan, W. Q. Duan, X. F. Zhang, X. S. Mei, *Materials*, 12(2019)3088
18. Y. Ding, Z. Dou, Y. Gao, X. Gao, H. Li and D. Liu, *Chin. J. Mater. Res.*, 31 (2017) 853-859.
19. Y. Ding, Z. Dou, Y. Gao, X. Gao, H. Li and D. Liu, *Mater. Rev.*, 31 (2017) 150-155.
20. X. Yang, J. Hu, N. Guo, C. He, Y. Zhang and J. Wang, *J. Chongqing Uni. Tech. (Nat. Sci.)*, 32 (2018) 132-137.